

## FERMI GBM OBSERVATIONS OF V404 CYG DURING ITS 2015 OUTBURST

P. A. JENKE<sup>1</sup>, C. A. WILSON-HODGE<sup>3</sup>, JEROEN HOMAN<sup>4,5</sup>, P. VERES<sup>1</sup>, M. S. BRIGGS<sup>1</sup>, E. BURNS<sup>1</sup>, V. CONNAUGHTON<sup>2</sup>, M. H. FINGER<sup>2</sup>, M. HUI<sup>3</sup>

<sup>1</sup>University of Alabama in Huntsville, Huntsville, AL 35805, USA, peter.a.jenke@nasa.gov

<sup>2</sup>Universities Space Research Association, Huntsville, AL 35805, USA.

<sup>3</sup>Marshall Space Flight Center, Huntsville, AL 35812, USA

<sup>4</sup>MIT Kavli Institute for Astrophysics and Space Research, 77 Massachusetts Avenue 37-582D, Cambridge, MA 02139, USA

<sup>5</sup>SRON, Netherlands Institute for Space Research, Sorbonnelaan 2, 3584 CA Utrecht, The Netherlands

### ABSTRACT

V404 Cygni was discovered in 1989 by the *Ginga* X-ray satellite during its only previously observed X-ray outburst and soon after confirmed as a black hole binary. On June 15, 2015, the Gamma Ray Burst Monitor (GBM) triggered on a new outburst of V404 Cygni. We present 13 days of GBM observations of this outburst including Earth occultation flux measurements, spectral and temporal analysis. The Earth occultation fluxes reached 30 Crab with detected emission to 100 keV and determined, via hardness ratios, that the source was in a hard state. At high luminosity, spectral analysis between 8 and 300 keV showed that the electron temperature decreased with increasing luminosity. This is expected if the protons and electrons are in thermal equilibrium during an outburst with the electrons cooled by the Compton scattering of softer seed photons from the disk. However, the implied seed photon temperatures are unusually high, suggesting a contribution from another source, such as the jet. No evidence of state transitions is seen during this time period. The temporal analysis reveals power spectra that can be modeled with two or three strong, broad Lorentzians, similar to the power spectra of black hole binaries in their hard state.

*Keywords:* V404 Cyg, black holes, LMXB

### 1. INTRODUCTION

V404 Cygni, hereafter V404 Cyg, was first identified as an X-ray transient with the *Ginga* satellite during the 1989 flaring event (Makino et al. 1989). Using archival optical data, V404 Cyg was associated with what was thought to be a nova in two previous outbursts in 1938 and 1956. Optical observations after the 1989 flaring event revealed an orbital ephemeris with an orbital period of 6.5 days, an inclination of 56 degrees, and most importantly a mass function of  $6.08 \pm 0.16 M_{\odot}$  (Casares and Charles 1994) making the source one of the first confirmed black hole systems with a black hole mass  $\sim 10 M_{\odot}$ . A radio parallax distance of  $2.39 \pm 0.14$  kpc (Miller-Jones et al. 2009) allows precise estimates of the intrinsic luminosity and makes this one of the closest known black hole systems. V404 Cyg's large separation from its companion along with optical H $\alpha$  observations indicate that the system develops a very large accretion disk which contains an inordinate amount of material ensuring dramatic flares when the inner region of the accretion disk breaks down (Remillard and McClintock 2006).

At 18:31:38 UT on 2015, June 15, the *Swift* Burst

Alert Telescope (BAT) triggered and located V404 Cyg (Barthelmy et al. 2015). Twenty eight minutes later, the *Fermi* Gamma Ray Burst Monitor (GBM) triggered on an X-ray source with a subsequent ground localization consistent with V404 Cyg.

### 2. GAMMA RAY BURST MONITOR

GBM is an all sky monitor whose primary objective is to extend the energy range over which gamma-ray bursts are observed in the Large Area Telescope (LAT) on *Fermi* (Meegan et al. 2009). GBM consists of 12 NaI detectors with a diameter of 12.7 cm and a thickness of 1.27 cm and two BGO detectors with a diameter and thickness of 12.7 cm. The NaI detectors have an energy range from 8 keV to 1 MeV while the BGOs extend the energy range to 40 MeV. GBM has three continuous data types: CTIME data with nominal 0.256-second time resolution and 8-channel spectral resolution used for event detection and localization, CSPEC data with nominal 4.096-second time resolution and 128-channel spectral resolution which is used for spectral modeling, and Continuous Time Tagged Event (CTTE) data which has a timing precision of  $2\mu\text{s}$ . All three data types are

utilized in the following analysis.

The GBM flight software was designed so that GBM can trigger on-board in response to impulsive events, when the count rates recorded in two or more NaI detectors significantly exceed the background count rate on at least one time-scale from 16 ms to 4.096 s in at least one of four energy ranges above 25 keV. The lower energy and longer time-scales are not used with the on-board triggering algorithms owing to strong variations in background rates that are incompatible with a simple background modeling needed for automated operation on a spacecraft.

### 3. OBSERVATIONS

GBM triggered on V404 Cyg 169 times between June 15-27. The source reached a brightness of 30 Crab with emission to 300 keV. With an 8 sr field of view, GBM was able to observe the entire outburst with a duty cycle of 57%. GBM is not an imaging instrument but uses the differential response of its 12 NaI detectors to locate sources to a few degrees (Connaughton et al. 2015). Even though localization is possible, GBM’s high background rates can make analysis challenging. To mitigate this limitation, three techniques are employed to analyze this source: the Earth occultation technique, choosing times of high signal to noise such as GBM triggered events, and using GBM’s  $2\mu\text{s}$  timing precision to extract temporal information from the data. These techniques and their results are detailed below.

#### 3.1. Earth Occultation Observations

The Earth Occultation software, described in detail in Wilson-Hodge et al. (2012), fits the GBM CTIME data with a quadratic background plus models of occultation steps for the source of interest and any other bright sources occulting during the 4-minute fit window. The occultation step models incorporate atmospheric transmission and an assumed source flux model for each source in the fit. Independent fits are performed for each detector and each energy channel. For V404 Cyg, the assumed flux model was based on INTEGRAL SPI measurements (Rodriguez et al. 2015). Steps during solar flares, and when the constant background term was more than  $3\sigma$  away from its Gaussian mean from pre-outburst data 2008 August to 2015 June 16 were removed from the analysis. High values of the constant term correlate with periods of high KP index (high particle activity). Figure 1 shows the light curve based on single occultation steps for V404 Cyg in the 8-300 keV band (GBM CTIME channels 0-4). V404 Cyg flux measurements in each energy channel were normalized to the average flux for the Crab nebula and pulsar for the time period 2015 June 17-July 2. Significant detections of a source within a single occultation step with GBM is

unusual and is an indication of how bright V404 Cyg’s flares were.

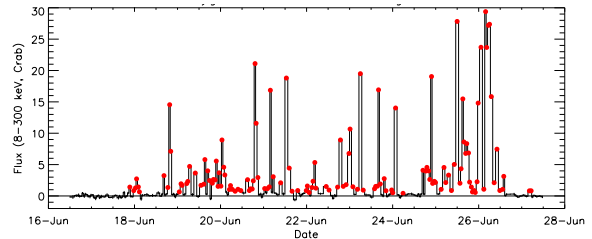


**Figure 1.** V404 Cyg light curve measured with Fermi GBM in the 8-300 keV band. Fluxes are normalized to GBM measurements of the Crab in the same band. Red circles indicate  $3\sigma$  or better detections in a single occultation step.

Remillard and McClintock (2006) described ways of defining black hole states, including a method based on radio properties, X-ray power density spectra, and hardness intensity diagrams. Hardness ratios were defined as 8.6-18.0 keV counts/5.0-8.6 keV counts measured with the *Rossi X-ray Timing Explorer (RXTE)* Proportional Counter Array, for which the Crab nebula yielded  $\text{HR}=0.68$ . Remillard and McClintock (2006) found that sources with  $\text{HR}>0.68$ , harder than the Crab Nebula, corresponded to the hard state in both McClintock and Remillard (2006) model and in the unified jet model (Fender et al. 2004) and  $\text{HR}<0.2$  corresponded to the steep power law state. Further discussion in Remillard and McClintock (2006), and references therein, points out that in the hard state, an exponential cutoff near 100 keV is often found, while QPOs may or may not be present. Remillard and McClintock (2006) emphasize that luminosity is not a criterion for identifying X-ray states in either prescription.

To compare GBM measurements of V404 Cyg to these studies, hardness ratios were generated by dividing the single step flux measured in the 12-25 keV band by the flux in the 8-12 keV band, the lowest two bands available in GBM data and closest to the canonical *RXTE* bands, shown in Figure 2. The majority of the GBM hardness ratios (blue diamonds in Figure 2) are harder than the Crab, suggesting that V404 Cyg spent the majority of its outburst in the hard state even though it was emitting at a large fraction of its Eddington luminosity.

#### 3.2. Spectral Analysis

During the hard state the BH disk is truncated and the inner region is filled with a hot ( $> 50$  keV) advection-dominated optically thin accretion flow typically referred to as the corona. There are many unanswered questions regarding the corona including its size, location, and shape but it is generally agreed that the high energy emission originates from the hot electrons up-scattering soft photons from the accretion disk. We

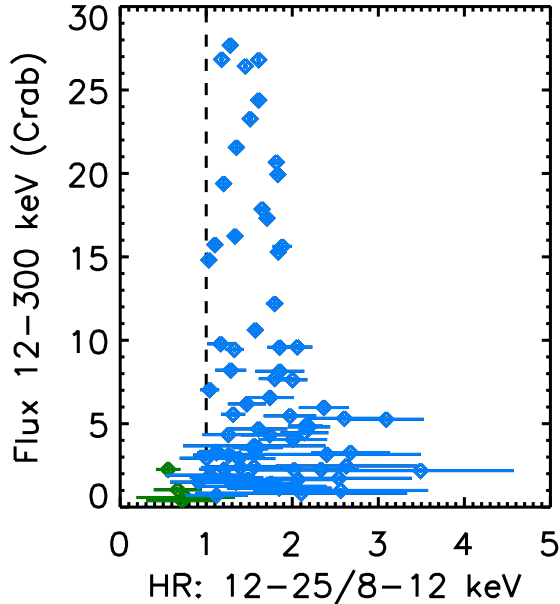


**Figure 2.** V404 Cyg hardness ratio (12-25 keV flux/8-12 keV flux) vs total flux in the 12-300 keV range. The dashed vertical line indicates the Crab hardness ratio for these bands. It is at 1.0 because the fluxes are normalized to the Crab. Blue diamonds indicate where V404 Cyg is harder than the Crab and green diamonds indicate where V404 Cyg is softer than the Crab.

performed spectral analysis of the hard X-ray emission between 8 and 1000 keV in order to better understand this hot Comptonized corona in the vicinity of the black hole.

### 3.2.1. Data Selection

2000s of GBM CSPEC data centered on the trigger times for all 169 triggers were selected for spectral analysis. Detectors with angles between the source and detector bore sight greater than 60 degrees were excluded. Using RMFIT, a forward-folding spectral analysis software often used in GBM gamma ray burst studies<sup>1</sup>, a polynomial background was fit to each detector in each energy channel between 8 and 1000 keV using times before and after the flare. Times around the trigger times, when a flare was evident, were chosen and response matrices were created from a response model constructed from simulations incorporating the Fermi spacecraft mass model into GEANT4 (Agostinelli and et al. 2003). Source selection was limited to 200 s in order to ensure that an adequate background model could be fit and that the spacecraft response would not significantly change during the times of data selection. The background subtracted data was fit using RMFIT to the CompST model (Sunyaev and Titarchuk 1980) and the

residuals in each detector were compared for consistency. Consistent residuals across detectors are an indication that the background selection is reasonable. Triggered events in which a good background model could not be constructed were rejected. For the remaining 155 events in which an acceptable spectral fit was possible, the background and the total spectrum were exported for analysis in XSPEC (Arnaud 1996).

### 3.2.2. Integrated Spectral Analysis Results

We chose spectral models to model the hot Comptonized corona surrounding the black hole. The CompTT model (Titarchuk 1994) and the REFLECT\*CompTT were successful in representing the data. The REFLECT\*CompTT model resulted in a reflection component that often dominated the spectrum where  $\Omega/2\pi \gg 1.0$ . The CompTT model alone resulted in a high seed photon temperature that averaged above 5 keV. We fixed the seed photon temperature to 1 keV and fixed the reflection amplitude to  $\Omega/2\pi = 1.0$  for the REFLECT\*CompTT model. In 130 out of 155 spectral fits we were able to reject (68% level and 110 out of 155 at the 95% level) the REFLECT\*CompTT in favor of the CompTT model with the high seed photon index. In addition the REFLECT\*CompTT model with amplitude and seed photon temperature fixed often resulted in a high ( $\bar{\tau} = 3.3$ ) optical depth.

We also choose the CUTOFFPL model for its simplicity but the model was less successful at representing the data. The high energy cut-off, at times, was much lower than the 100 keV often observed for stellar mass black hole systems in the hard state (Malzac 2012; Remillard and McClintock 2006) and often near GBM's low energy threshold resulting in fits with unconstrained parameters and very hard indexes. Nevertheless, the CUTOFFPL is useful for tracing the spectral variability between triggered flares and there is no evidence for systematic softening or hardening of the spectrum during this period.

The CompTT model seed photon temperature,  $kT_{\text{photon}}$ , is a free parameter and allows us to probe emission from the up-scattering of hot seed photons as apposed to the CompST model which assumes a cold distribution of seed photons. The CompTT model fits resulted in an average seed photon temperature of  $5.9 \pm 1.3$  keV consistent with INTEGRAL observations (Natalucci et al. 2015; Roques et al. 2015). This high photon seed temperature is inconsistent with photons from an accretion disk ( $kT_{\text{photon}} < 1$  keV) and the cold photons assumed in the CompST model. The average optical depth,  $\tau$ , is  $1.45 \pm 1.0$  ( $\sigma_{\tau} = 0.56$ ) (see Figure 3) which is consistent with the moderate electron temperatures measured for this source (Droulans et al. 2010; Malzac 2012).

<sup>1</sup> <http://fermi.gsfc.nasa.gov/ssc/data/analysis/rmfilt/>

The results for the CompTT model are summarized in Figure 3 and detailed in the online table. The  $\chi^2$  could be improved by ignoring the energy band between 30 and 40 keV where there is a poorly modeled K-edge. The K-edge does not affect the spectral results only the quality of the fit and removing those energy bins makes it more difficult to constrain the parameters. There does not appear to be any evolution in the spectral parameters that would signify a state change.

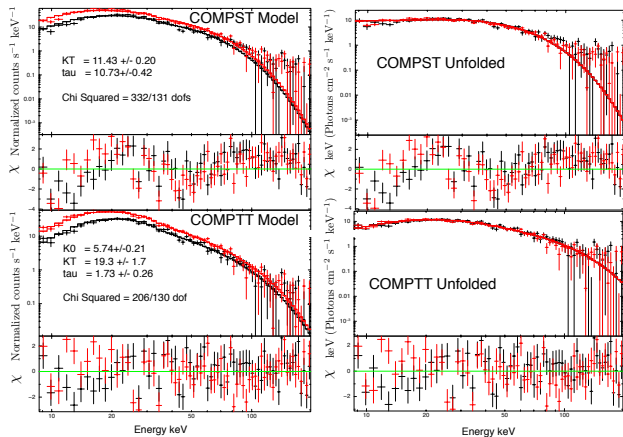


**Figure 3.** Time integrated spectral model fitting the triggered event bn150626171 using 12 seconds of triggered data. The figure on the top left is the spectral fit using the CompST model with residuals below. The red and black points are the normalized counts from two of the NaI detectors while the red and black curves are the best fit model. The figure on the bottom left is the spectral fit using the CompTT model with residuals below. The best fit parameters are given in the figures. The figures on the right are the same fit results as the left except shown as the unfolded spectrum ( $E F(E)$ ). The fit for the CompTT model is a significant improvement over the CompST model.

### 3.2.3. Time Resolved Spectral Analysis Results

Time resolved spectral analysis was performed on a few bright triggered flares to examine spectral variation within a flare. Ten second intervals were used for the time resolved analysis and an instrument response matrix was created for the centroid of each time interval. Only the CompTT model was used to fit the time resolved data. The trigger bn150625400 was chosen because it spanned a wide range of luminosities. The triggers bn150626685 and bn150626751 were chosen for their high luminosity while bn150626156 was chosen for its moderate luminosity. For the individual triggers, the optical depth varied very little therefore the optical depth was frozen at the best parameter fit from the time integrated spectral analysis. Figure 5 shows how the electron and photon temperature evolve during the bright flare, bn150625400. There is only a small segment of time between 280 and 350 s where the electron temperature and photon temperature appear correlated.

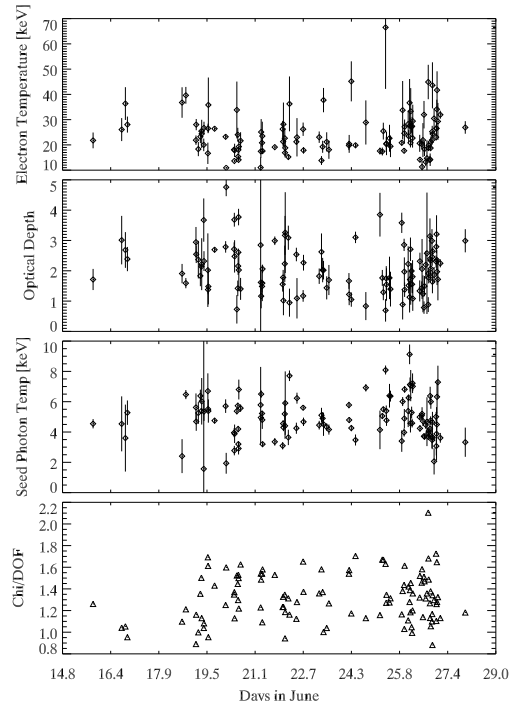


**Figure 4.** Time integrated spectral results for each triggered event specified by days in June. Only the results where the electron temperature can be constrained are shown. The top panel is the electron temperature which generally varies between 10–40 keV. The panel below is the optical depth which varies between 1 and 4. The third panel is the seed photon temperature which varies between 2 and 8 keV. The last panel shows the reduced  $\chi^2$  for the fit. For GBM data, anything below 1.6 is considered a successful fit.

## 3.3. Temporal Data Analysis

### 3.3.1. Data Selection

GBM CTTE NaI data between 8 and 100 keV were selected between 2015 June 15–27. Times during SAA passage, times when V404 Cyg was occulted by the Earth and times during high particle activity were excluded from the analysis. The data selection resulted in good time intervals (GTIs) that were a few  $\times 1000$  seconds long. On a 100 second cadence, the selected CTTE data were combined for all the detectors which had a source to detector bore sight angle of less than 60 degrees, and binned to 1 ms, to produce 100 second long light curves. The light curves were Fourier transformed producing power spectra with a frequency range of 0.01–500 Hz. The power spectra for each GTI were averaged to reduce the variance resulting in 214 power spectra.

Although source and background count rates were not available for all observations, the power spectra that were studied in detail (see below), were all rms normalized (Belloni and Hasinger 1990; Miyamoto et al. 1991). We note, however, that the source and background rates used for the rms normalization are estimates based on the spectral analysis.



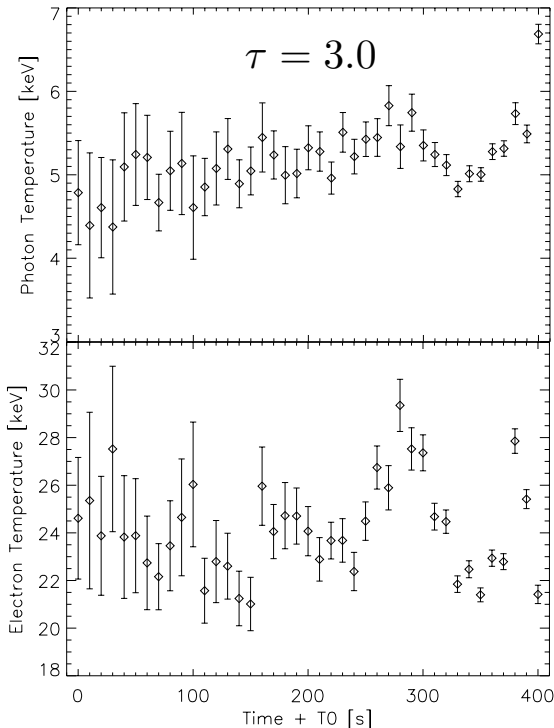


**Figure 5.** The top figure shows the evolution of the photon seed temperature during the GBM triggered flare, bn150625400, while the bottom figure shows the evolution of the electron temperature. The horizontal axis is time in seconds with T0 = 2015-06-25 09:33:43.6 UT. The optical depth,  $\tau$ , is fixed to the best fit time integrated value.

### 3.3.2. Temporal Analysis Results

All 214 power spectra were visually inspected. For the ones from low-count-rate observations no significant power is seen. However, the power spectra from observations during bright flares are of high quality and show significant power. In Figure 6 we show five normalized power spectra from the period of June 26–27, during which the source reached its peak brightness. They are representative of the power spectra during other flares. The power spectra are dominated by strong broad features, similar to *Ginga* power spectra of V404 Cyg during its 1989 outburst (Oosterbroek et al. 1997). No narrow QPO features were seen. The integrated fractional rms in the 0.01–100 Hz band ranged from  $\sim 35\%$  to  $\sim 50\%$ .

Like the *Ginga* power spectra, we find that the Fermi/GBM power spectra of V404 Cyg can be fitted well with two or three broad Lorentzians, where we define the Lorentzians as  $(P(\nu) = (r^2\Delta/\pi)[\Delta^2 + (\nu - \nu_0)^2]^{-1})$ . Here  $\nu_0$  is the centroid frequency,  $\Delta$  the half-width-at-half-maximum, and  $r$  the integrated fractional rms (from  $-\infty$  to  $\infty$ ). Instead of  $\nu_0$  and  $\Delta$  we will quote the frequency  $\nu_{max}$  at which the Lorentzian at-

tains its maximum in  $\nu P(\nu)$  and the quality factor,  $Q$ , where  $\nu_{max} = \nu_0(1 + 1/4Q^2)^{1/2}$  and  $Q = \nu_0/2\Delta$ . In some cases an additional power-law at low-frequencies provides a minor improvement to the fits, but for reasons of consistency this component was left out of our final model.

The Lorentzian fits to the power spectra are shown in Figure 6. As can be seen, the Lorentzians are well-separated in frequency. Small shifts in the frequencies of the Lorentzians are seen, but the overall shape of the power spectra remained the same, with perhaps an exception in the bottom panel of Figure 6. This was also mostly the case for the *Ginga* power spectra reported by Oosterbroek et al. (1997), who only observed one clear exception from the usual shape in their set of power spectra. The  $\nu_{max}$  ranges for the three Lorentzians are:  $\sim 0.016$ – $0.04$  Hz,  $\sim 0.47$ – $0.87$  Hz, and  $\sim 2.7$ – $4.8$  Hz. The  $Q$ -values of the broad noise features were less than 0.8 and in most cases were fixed at 0. The fractional rms amplitudes of the low-, mid-, and high-frequency Lorentzians were  $\sim 31$ – $36\%$ ,  $\sim 16$ – $28\%$ , and  $\sim 15$ – $23\%$ , respectively. The full list of fit parameters is given in Table 1. Note that the quality of the June 27 power spectrum in Figure 6 was not high enough to separately fit the two highest-frequency components, and only two Lorentzians were used to fit this power spectrum.

## 4. DISCUSSION

For a  $10M_{\odot}$  black hole the Schwarzschild radius is  $R_S = 3 \times 10^6$  cm and the Eddington luminosity is  $L_{EDD} = 1.26 \times 10^{39}$  erg s $^{-1}$ . The luminosities calculated for GBM data are from 10–1000 keV. Significant flux is expected below 10 keV therefore our luminosities represent lower limits to the bolometric luminosity. It is probable that V404 Cyg reached or exceeded the Eddington luminosity during the 2015 outburst.

### 4.1. Spectral Modeling

Initially a comptonized model by Sunyaev and Titarchuk (1980) (CompST in XSPEC) was chosen to model the emission from hot coronal electrons up-scattering the cold accretion disk photons. This model was chosen for its small number of parameters and its physical description of the emission region. The model was often a poor description of the GBM data, especially during bright flares, and resulted in a large optical depth, tau (see Figure 3) which is inconsistent with the low electron temperatures. Two absorption models, PHABS and PCFABS in XSPEC, were used to improve the model fit. Both absorption models predicted extremely high absorption  $((100 - 1000) \times 10^{22}$  cm $^2$ ) that is unsupported by soft X-ray observations (Motta et al. 2015). A reflection model (REFLECT in XSPEC) was also used to attempt to improve the CompST fit. The in-

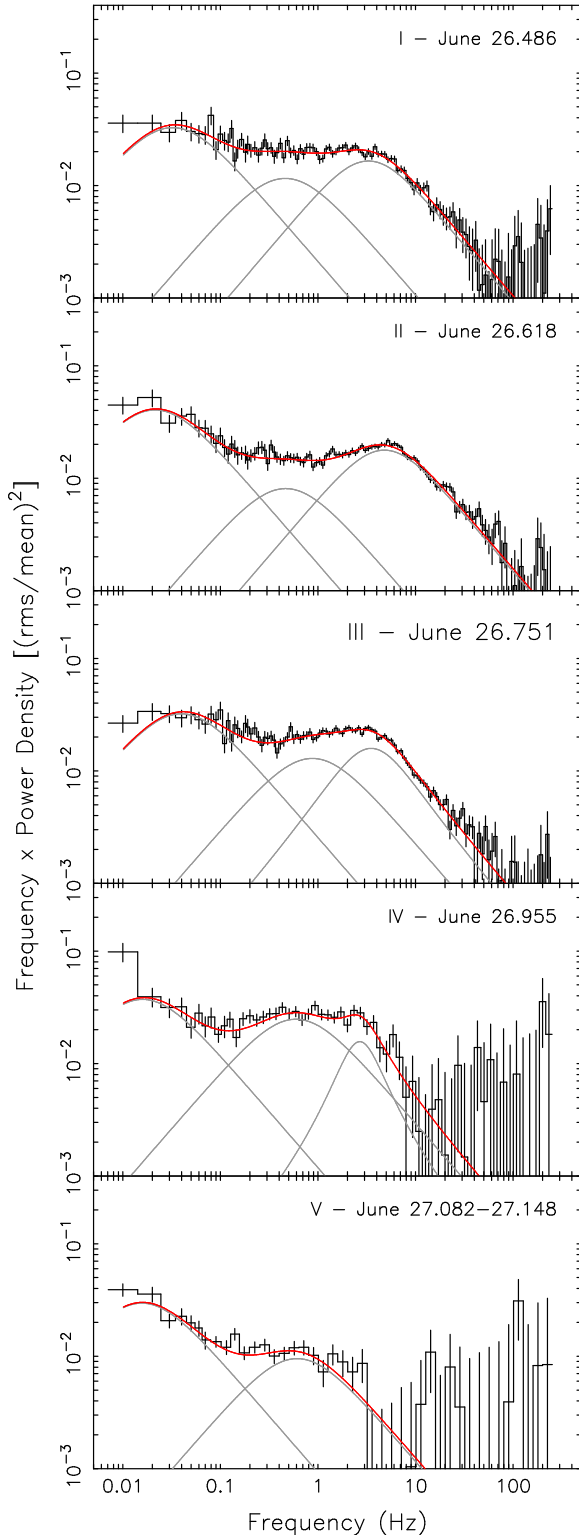


**Figure 6.** A sequence of five power spectra of V404 Cyg from June 26–27. Models fits with two or three Lorentzian are shown in red; individual Lorentzians are plotted in gray. Corresponding dates are shown in the upper right corners. See Table 1 for fit parameters.

clination of the the accretion disc was fixed to 56 degrees (Khargharia et al. 2010) and the redshift fixed to zero reflecting our proximity to the source. The new model was again preferred over just the CompST model but resulted in an unphysical reflection component which exceeded the unreflected component which requires extreme relativistic light bending (Fabian 2013). Other issues with the REFLECT\*CompST model was, again, an excessively large optical depth that was often greater than 10. The CompST model was abandoned in favor of the more flexible CompTT model.

The CompTT model resulted in a seed photon temperature that was too hot to originate from the accretion disk. Including a reflection model and fixing the seed photon temperature to 1 keV resulted in reasonable fits for GBM data but the reflection component was often unphysically large ( $\Omega/2\pi \gg 1$ ) as well as the optical depth ( $\bar{\tau} = 3.3$  with reflection as apposed to  $\bar{\tau} = 1.6$  without reflection). The spectrum from V404 Cyg has significant curvature around 20 keV which, assuming a comptonized model, may be fit with a high seed photon temperature or scattering a large number (on the order of the number of photons in the unreflected spectrum from 8 - 100 keV) of high energy photons down to lower energy and into the observers line of sight. By fixing the reflection amplitude to 1.0 and fixing the seed photon temperature to 1.0 keV we refit all the spectra and compared the results to the CompTT fit with no reflection and the seed photon temperature as a free parameter. Overall the CompTT model with the high seed photon temperature resulted in a better fit to the data. Investigating further, we took the 12 seconds of the triggered event bn150626171 (see Figure 3) and simulated 1000 sets of spectra (for detector n9 and na) using the best fit CompTT parameters. We then simulated 1000 sets of spectra for the best fit parameters of the REFLECT\*CompTT model with the reflection amplitude and seed photon temperature fixed as before. Comparing the  $\Delta\chi^2$  of the resulting fits, all but a few of the fits using the REFLECT\*CompTT model were rejected at the 99% level and none resulted in a lower  $\chi^2_{\nu}$  (see Figure 7). Although not statistically rigorous, the results are compelling enough that we can not reject the hot seed photons of the CompTT model.

Relativistic light bending when the emission region is within a few gravitational radii of the black hole can produce reflection that exceeds  $\Omega/2\pi = 1$  (Fabian 2013). Fixing the reflection to  $\Omega/2\pi = 1.5$  to take into account a large degree of relativistic light bending still results in a photon seed temperature that is consistently above 2 keV and averages 3.7 keV as opposed to 5.1 keV with no reflection. Unfortunately we are unable to constrain both the reflection and the electron seed temperature. Even though it is likely that there is a reflection com-

ponent (Chandra observed broadened Fe K $\alpha$  lines, see King et al. (2015)), GBM is not sensitive enough to constrain the reflection excess. The addition of the reflection component lowers the seed photon temperature for the REFLECT\*CompTT fits by a marginal amount but does not alter the conclusion that these photons are too hot to be the thermal photons expected from an accretion disk. Absorption might improve the spectral fits resulting in a thermal seed photon distribution but the absorption required is at least 100 times Galactic and neither XMM-Newton (Rana et al. 2015) nor Chandra (King et al. 2015) observed excessive absorption. Absorption a few times Galactic will have little effect on our spectra above 8 keV so we omitted absorption in our spectral fits.

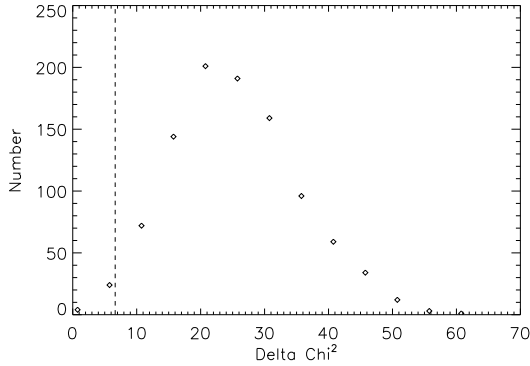


**Figure 7.** The distribution of the  $\Delta\chi^2$  of the REFLECT\*CompTT and CompTT model. The dashed line is the 99% rejection point. The REFLECT\*CompTT model can be rejected in all but the six simulated spectra.

#### 4.2. Physical Model for the Hard X-ray Emission

We find a clear anti-correlation between the GBM flux and the electron temperature of the CompTT model. We present this behavior in the equivalent  $L/L_{\text{EDD}} - kT_e$  diagram. This correlation is present both in the brighter flares (see Figures 9,10,11) and when considering the entire duration of the current V404 Cyg flaring activity (see Figure 8).

Overall, the electron temperature values show large variations and no obvious correlation up to  $L \lesssim 0.2L_{\text{EDD}}$ . For  $L > 0.2L_{\text{EDD}}$  a clear anti-correlation emerges, and the scatter in  $T_e$  decreases visibly (see Figure 8). Individual outbursts show a similar behavior, when well sampled (trigger bn150625400 in Figure 9).

The correlation between the electron temperature and luminosity has already been noted in the case of GX 339-4 by Miyakawa et al. (2008). Using GBM observations of V404 Cyg, we can populate a larger swath of the  $L - kT_e$  diagram and find their interpretation valid here as well with minor modifications. We envision a popula-

tion of protons in thermal equilibrium with hot electrons which are in turn responsible for the inverse Compton up-scattering of the soft thermal photons from the disk or base of the jet, resulting in the gamma-ray photons.

In order to determine which processes drive the bursting activity, we calculate relevant timescales. For a case when protons have non-relativistic temperatures electron-proton relaxation timescale can be calculated as (Spitzer 1962; Dermer 1986):

$$t_{pe} \approx \frac{\sqrt{2\pi} \left( \frac{kT_p}{m_p c^2} + \frac{kT_e}{m_e c^2} \right)^{\frac{3}{2}}}{2n_e \sigma_T c \ln \Lambda} \frac{m_p}{m_e} \approx \quad (1)$$

$$\approx 1.3 \times 10^{-3} \left( \frac{R}{10 R_S} \right) \left( \frac{kT_e}{30 \text{ keV}} \right)^{\frac{3}{2}} \left( \frac{\tau}{1.6} \right)^{-1} \text{ s}, \quad (2)$$

where  $n_e$  is the particle number density,  $\ln \Lambda = 16.1 + \ln[(kT_e/30\text{keV})(n_e/10^{17}\text{cm}^{-3})^{-1/2}]$  is the Coulomb logarithm,  $T_e$  and  $T_p$  are the electron and proton temperatures respectively. Electrons and protons establish a Maxwellian distribution on this timescale. For the numerical value, we have assumed  $T_e > \frac{m_e}{m_p} T_p$  and  $\tau \approx R n_e \sigma_T$ . Henceforth, we use  $10R_S$  for the size of the emission region.

Electrons will lose energy to soft photons through inverse Compton scattering on a timescale

$$t_{\text{IC}} = \frac{3m_e c}{8\sigma_T u_\gamma \tau} \quad (3)$$

$$= 10^{-6} \left( \frac{L/L_{\text{EDD}}}{0.2} \right)^{-1} \left( \frac{f}{9} \right)^{-1} \left( \frac{R}{10 R_S} \right)^2 \left( \frac{\tau}{1.6} \right)^{-1} \quad (4)$$

where  $u_\gamma = Lf/4\pi R^2 c$  is the energy density of soft photons entering the corona,  $f$  is the ratio between the luminosity of the soft, disk component ( $L_s$ ) and the up-scattered hard X-ray luminosity, observed by GBM ( $L$ ).  $f$  follows e.g. from the derivation of Pietrini and Krolik (1995), and yields  $f = L_s/L \approx (10\theta_e \tau)^{-4} \gtrsim 9$ , and approximately constant for luminosities above  $0.2L_E$  where  $\theta = kT_e/m_e c^2$ .

The advection timescale, or the time in which electrons are swallowed by the black hole (Mahadevan and Quataert 1997) can be calculated e.g. in the advection dominated accretion flow model (Narayan and Yi 1994):

$$t_{\text{adv}} \approx \frac{R^2}{\alpha H^2 \sqrt{GM/R^3}} \quad (5)$$

$$= 0.4 \left( \frac{R/H}{0.2} \right)^2 \left( \frac{R}{10 R_S} \right)^{3/2} \left( \frac{\alpha}{0.3} \right)^{-1} \text{ s}, \quad (6)$$

where  $H$  is the height of the disk, assumed to be a fraction 0.2 of the radius, and  $\alpha$  is the viscosity parameter scaled to 0.3.

Out of these three timescales, the Compton cooling is the shortest. Based on the above equations the proton-

electron equilibrium timescale is shorter than the advection timescale indicating the former is the more efficient process. However the value of  $H$ ,  $\alpha$  and the emission region size assumed here,  $10R_S$  have large uncertainties allowing  $t_{\text{adv}}$  to be of the same order as  $t_{\text{pe}}$  (e.g. for  $H/R \approx \alpha \approx 1$ , and  $R \approx 3R_S$ ). If this is the case, about an equal fraction of proton energy will be available to **the electrons for IC up scattering and for advection**. As the luminosity increases, IC cooling becomes more effective, decreasing the temperature of the electrons. Colder electrons result in more effective proton-electron collisional relaxation, while the advection efficiency does not vary with electron temperature. Thus eventually the two main processes will be the electron proton interaction and the IC cooling of the electrons.

If we assume a steady state, the energy transferred per unit volume and unit time from protons to electrons will equal the energy lost by electrons through Compton cooling. Following Inoue (1994); Miyakawa et al. (2008), yields:

$$\frac{3/2n_e kT_p}{t_{\text{pe}}} = 4\theta_e u \gamma n_e \sigma_{TC}. \quad (7)$$

From Equation 7, using the expression for  $t_{\text{pe}}$ , we find  $T_e \propto L^{-2/5}$ , which is in remarkable agreement with both the time resolved spectra (see Figures 9,10,11) and considering all the bursts (see Figure 8).

Here, we neglected variation of the proton temperature and optical depth. Since the proton-electron heating timescale is shorter than the advection timescale, in the absence of heating, the protons might cool down to lower temperatures before being advected. To see if the proton temperature is independent of other parameters (e.g. the luminosity) we calculate it following Malzac and Belmont (2008) by defining the Coulomb compactness, neglecting pair contributions:

$$l_C = \sqrt{8\pi}\tau^2 \ln \Lambda \frac{k(T_p - T_e)}{m_p c^2} \left( \frac{kT_p}{m_p c^2} + \frac{kT_e}{m_e c^2} \right)^{-3/2}. \quad (8)$$

We fix  $l_C = 473$  by using the average  $\tau = 1.95$ ,  $T_e = 26$  keV and  $T_p = 46$  MeV (from  $GM/R = kT_p/m_p$ ,  $R = 10R_S$ ), then solve for the proton temperature in the  $kT_p/m_p c^2 \ll 1$  limit. We get  $T_p = T_e(1 + 8.6\sqrt{7\theta_e}l_C/\tau^2)$ . The average of the proton temperatures is  $\langle T_p \rangle = 15.2$  MeV, indeed somewhat lower than from the virial type energy considerations but higher than Droulans et al. (2010). The Pearson correlation coefficient between  $\log L$  and  $\log T_p$  is 0.14, with p-value  $p=0.11$ , consistent with no correlation between  $L$  and  $T_p$ . This method of determining  $T_p$  is appropriate for an estimate and for checking correlation with the luminosity. Unfortunately, it uses the same principle by which we link  $t_{\text{pe}}$  to the electron temperature and hence renders equation 7 meaningless (yields  $T_p \propto T_e^{3/2}$ ) for the

purpose of further addressing the electron temperature - luminosity correlation.

GBM is not sensitive to photons below  $\sim 8$  keV. Some fraction of the bolometric luminosity is emitted at this range and it is difficult for us to account for that (but see f parameter at the beginning of this section for an estimate). Pair annihilation represents only a few percent (Siebert et al. 2016) of the overall luminosity and is also not considered here. We can simply equate the luminosity observed by GBM ( $L$ ) in a spherical volume of  $10 R_S$ , assumed to be dominated by Comptonized emission, to the collisional power of the protons ( $\frac{3}{2}nkT_p/t_{\text{pe}}$ ). This will yield

$$kT_e = 36.2\text{keV} \left( \frac{L}{0.2L_E} \right)^{-2/3}. \quad (9)$$

We derived the normalization assuming  $T_p = 16$  MeV,  $n = 10^{17} \text{ cm}^{-3}$ . The power law index is steeper than the fitted value, but still consistent within the errors. Moreover, the expression in equation 9 gives a good description of the data, especially at high luminosities.

This observed relation between the electron temperature and luminosity suggests that during an outburst the electrons and protons are in thermal equilibrium and the electrons are cooled by the Compton scattering of thermal photons from the disk. V404 Cyg is yet another example among accreting black hole systems (both black hole binaries and AGN) where the collisional heating of electrons by protons is a dominant process.

*Alternative models.* Alternatively the anticorrelation between the luminosity and electron temperature can be investigated considering runaway pair production (e.g. Fabian et al 2015). This occurs for high compactness and electron temperature as additional power introduced to the corona does not go towards increasing the temperature but to the creation of pairs. Defining the compactness,  $l = \sigma_T L/m_e c^3 R = 2\pi m_p/m_e (L/L_E)(R/R_S)^{-1}$ , for a spherical corona, we have a limit corresponding to  $l \approx 10\theta_e^{-5/2}e^{1/\theta_e}$ . We have also adopted the model of Stern et al 1995 who calculated the pair line for a slab geometry. We assume  $3R_S$  for the height and the radius of the slab and sphere cases respective. Larger sizes will be less constraining. We have plotted the runaway pair production lines for sphere and slab geometry on Figure 8. We conclude that our observations do not violate this limit for realistic assumptions for the emission radius, but this effect does not seem to drive the observed correlation. Another possibility to consider is the truncated disk model (Done et al. 2007; Sobolewska et al. 2011). In this model the disk is truncated at an inner radius, and hot, spherical corona fills the space closer to the black hole. With increasing luminosity, the disk truncation radius decreases. This results in more effective



cooling of the hot corona by disk photons. Similar to Sobolewska et al. (2011), we consider a radiatively efficient and inefficient flow (Sharma et al. 2007) and link the hard-to-soft luminosity ratio (equivalent to the hard to soft compactness ratio) to the hard luminosity. We further use the expression of Pietrini and Krolik (1995) for the linking the hard-to-soft luminosity ratio to the temperature ( $L/L_s \propto (\theta_e \tau)^4$ , see previous section.) In this model we find  $L/L_s \propto L^{-1/4} (\propto L^{-3/2})$  in the radiatively inefficient (efficient) flow case. For the temperature dependence, assuming constant optical depth, we find  $L \propto T_e^{-1/8}$  for the inefficient flow and  $L \propto T_e^{-3/8}$  for the efficient flow. The latter, radiatively efficient flow case is consistent with our observed correlation at high luminosities suggesting the truncated disk model is viable in explaining the observations.

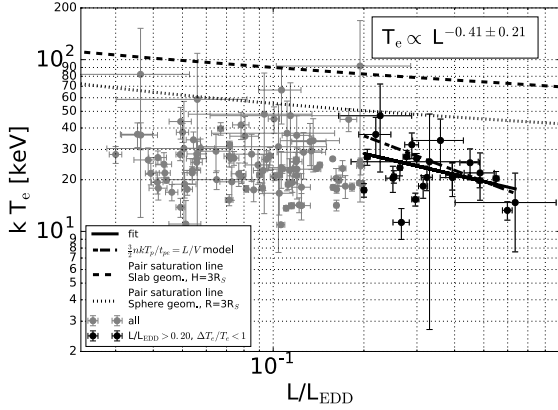


**Figure 8.** Luminosity,  $L/L_{\text{EDD}}$ , and electron temperature for all the triggered intervals. Gray points mark all the intervals, black points indicate bright ( $L > 0.2L_{\text{EDD}}$ ) and reliable fits ( $\chi^2_{\mu} < 2$ ).

Similarly to Roques et al. (2015), the seed photon temperature obtained from the CompTT model is unusually high. The highest temperature from a thermally radiating disk is  $kT_{\text{photon}} \lesssim 1$  keV, while we have an approximately constant  $kT_{\text{photon}} = 5.9 \pm 1.3$  keV. This suggests the seed photons might not originate solely from the disk, but from another source as well (e.g. synchrotron photons from the jet (Markoff et al. 2005)). A high seed photon temperature (7 keV) was also measured using INTEGRAL data (Roques et al. 2015; Natalucci et al. 2015).

We note that for the time resolved spectra the onset of the correlation appears to start at higher luminosities

( $0.35 - 0.5L_{\text{EDD}}$ , (see Figures 9, 10, 11) while the time integrated correlation is valid for  $L > 0.2L_{\text{EDD}}$ . This can be explained by the longer integration times for the data points ( $\sim 500$ s as apposed to 10s), resulting in more accurate spectral parameters for  $L/L_{\text{EDD}}$  in the range

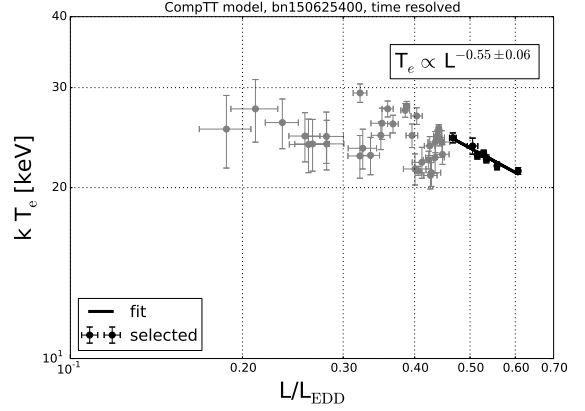


**Figure 9.** Luminosity,  $L/L_{\text{EDD}}$ , and electron temperature for an individual trigger. Gray points mark all the intervals, black points indicate bright ( $L > 0.5L_{\text{EDD}}$ ) and reliable fits ( $\chi^2_{\mu} < 2$ ).

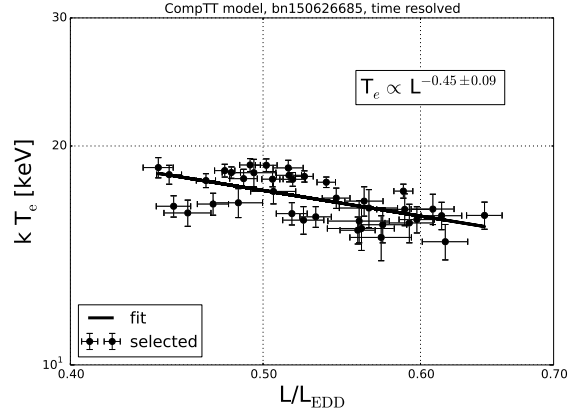


**Figure 10.** A further example of a time resolved fit. The anti-correlation exists for the entire flare because it remained above  $0.45L_{\text{Edd}}$ .

of 0.2-0.35. For the time resolved cases the error on the parameters increases for this range of luminosities, suppressing the correlation until sufficient photons are measured. Restricting the  $L/L_{\text{EDD}} > 0.4$  substantially steepens the relationship for the time integrated results.

### 4.3. Temporal Analysis

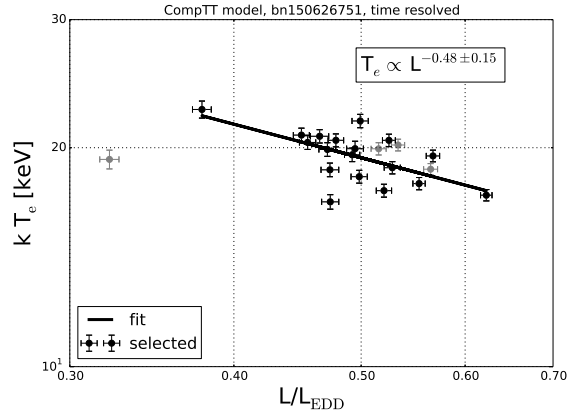


**Figure 11.** Luminosity,  $L/L_{\text{EDD}}$ , and electron temperature for individual triggers. Gray points mark all the intervals, black points indicate bright ( $L > 0.5L_{\text{EDD}}$ ) and reliable fits ( $\chi^2_{\mu} < 2$ ).

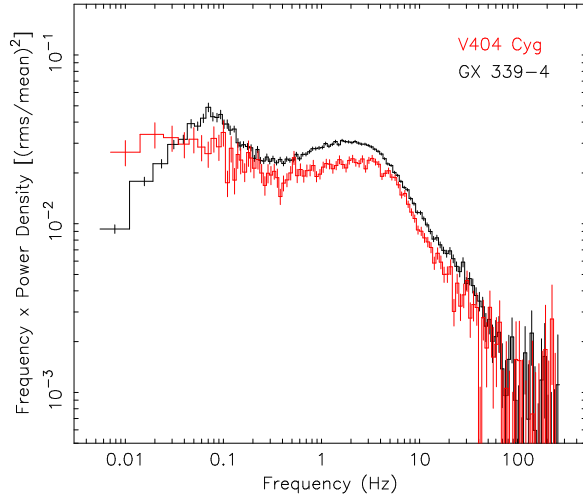


**Figure 12.** A comparison of an averaged *RXTE* power spectrum from the hard state of GX 339-4 (black) with a Fermi/GBM power spectrum of V404 Cyg from June 26.751 (red).

**Table 1.** Power Spectral Fit Parameters

PDS No. <sup>a</sup>	L <sub>low</sub>			L <sub>mid</sub>			L <sub>high</sub>		
	$\nu_{\text{max}}$ (Hz)	$Q$	rms (%)	$\nu_{\text{max}}$ (Hz)	$Q$	rms (%)	$\nu_{\text{max}}$ (Hz)	$Q$	rms (%)
I	$(3.2 \pm 0.6) \times 10^{-2}$	0 <sup>b</sup>	32.1 ± 1.5	0.46 ± 0.10	0 <sup>b</sup>	19.1 ± 1.0	3.3 ± 0.3	$(8 \pm 6) \times 10^{-2}$	22.0 ± 1.1
II	$(2.1 \pm 0.5) \times 10^{-2}$	0 <sup>b</sup>	36 ± 3	0.47 ± 0.08	0 <sup>b</sup>	15.9 ± 0.7	4.78 ± 0.16	$(7 \pm 3) \times 10^{-2}$	23.0 ± 0.4
III	$(4.0 \pm 0.5) \times 10^{-2}$	0 <sup>b</sup>	31.8 ± 1.2	0.87 ± 0.15	0 <sup>b</sup>	15.9 ± 0.7	3.5 ± 0.2	$(2.8 \pm 0.5) \times 10^{-1}$	19.6 ± 1.4
IV	$(1.6 \pm 0.6) \times 10^{-2}$	0 <sup>b</sup>	34 ± 5	0.59 ± 0.10	0 <sup>b</sup>	27.9 ± 1.3	2.7 ± 0.3	$(8 \pm 4) \times 10^{-1}$	15 ± 3
V	$(1.6 \pm 0.5) \times 10^{-2}$	0 <sup>b</sup>	31 ± 4	0.61 ± 0.10	0 <sup>b</sup>	17.3 ± 0.6	...	...	...

Table 1 continued

Table 1 (continued)

PDS No. <sup>a</sup>	L <sub>low</sub>			L <sub>mid</sub>			L <sub>high</sub>		
	$\nu_{\max}$ (Hz)	$Q$	rms (%)	$\nu_{\max}$ (Hz)	$Q$	rms (%)	$\nu_{\max}$ (Hz)	$Q$	rms (%)

<sup>a</sup> Number of power spectrum, as shown in Figure 6.

<sup>b</sup> Value was fixed.

The Fermi/GBM power spectra of V404 Cyg show a strong similarity to those obtained with *Ginga* during the source's 1989 outburst. They are also similar in shape and strength to those of black hole X-ray binaries, such as Cyg X-1 and GX 339-4, in their hard states (Nowak 2000). The power spectra of these source are dominated by broad Lorentzians as well, in the frequency range that we analyzed for V404 Cyg (0.01–500 Hz). In Figure 12 we show a comparison between an averaged power spectrum from GX 339-4 in its hard state (from *RXTE* data) and one from V404 Cyg (June 26.71, see middle panel in Figure 6). As can be seen, the shapes of these power spectra are very similar, especially at the high-frequency end. We suspect that relatively stronger variability at the low-frequency end in V404 Cyg may be the result of the strong flaring activity of V404 Cyg seen on the corresponding time scales. This additional power may hide the low-frequency break that is usually seen in the hard state (see, e.g., the GX 339-4 power spectrum in Figure 12). Overall, however,

the shape and strength of the power spectra supports our earlier conclusion that V404 Cyg was observed in the hard state.

## 5. CONCLUSION

There is no evidence in the spectral analysis for an onset of a state change during the observed time interval. Spectral analysis indicates that the collisional heating of electrons by protons is the dominant process resulting in the observed Comptonized spectrum. The seed photon temperature exceeds what is expected from an accretion disk and may be due to synchrotron photons from the base of the jet or perhaps there is some other method of energizing the photons of the inner disk. In all, this outburst is very similar to the one that occurred in 1989 but remains remarkable among black hole outburst for its intrinsic high luminosity and high photon seed temperature.

## REFERENCES

- Agostinelli, S. and et al.: 2003, *Nuclear Instruments and Methods in Physics Research Section A: Accelerators, Spectrometers, Detectors and Associated Equipment* **506(3)**, 250
- Arnaud, K. A.: 1996, in G. H. Jacoby and J. Barnes (eds.), *Astronomical Data Analysis Software and Systems V*, Vol. 101 of *Astronomical Society of the Pacific Conference Series*, p. 17
- Barthelmy, S. D., Chester, M. M., Malesani, D., and Page, K. L.: 2015, *GRB Coordinates Network* **17949**, 1
- Belloni, T. and Hasinger, G.: 1990, *A&A* **227**, L33
- Casares, J. and Charles, P. A.: 1994, in S. Holt and C. S. Day (eds.), *The Evolution of X-ray Binaries*, Vol. 308 of *American Institute of Physics Conference Series*, p. 107
- Connaughton, V., Briggs, M. S., Goldstein, A., Meegan, C. A., Paciesas, W. S., Preece, R. D., Wilson-Hodge, C. A., Gibby, M. H., Greiner, J., Gruber, D., Jenke, P., Kippen, R. M., Pelassa, V., Xiong, S., Yu, H.-F., Bhat, P. N., Burgess, J. M., Byrne, D., Fitzpatrick, G., Foley, S., Giles, M. M., Guiriec, S., van der Horst, A. J., von Kienlin, A., McBreen, S., McGlynn, S., Tierney, D., and Zhang, B.-B.: 2015, *ApJS* **216**, 32
- Dermer, C. D.: 1986, *ApJ* **307**, 47
- Done, C., Gierliński, M., and Kubota, A.: 2007, *A&A Rv* **15**, 1
- Droulans, R., Belmont, R., Malzac, J., and Jourdain, E.: 2010, *ApJ* **717**, 1022
- Fabian, A. C.: 2013, in C. M. Zhang, T. Belloni, M. Méndez, and S. N. Zhang (eds.), *Feeding Compact Objects: Accretion on All Scales*, Vol. 290 of *IAU Symposium*, pp 3–12
- Fender, R. P., Belloni, T. M., and Gallo, E.: 2004, *MNRAS* **355**, 1105
- Inoue, H.: 1994, in T. Courvoisier and A. Blecha (eds.), *Multi-Wavelength Continuum Emission of AGN*, Vol. 159 of *IAU Symposium*, pp 73–82
- Khargharia, J., Froning, C. S., and Robinson, E. L.: 2010, *ApJ* **716**, 1105
- King, A. L., Miller, J. M., Raymond, J., Reynolds, M. T., and Morningstar, W.: 2015, *ApJL* **813**, L37
- Mahadevan, R. and Quataert, E.: 1997, *ApJ* **490**, 605
- Makino, F., Wagner, R. M., Starrfield, S., Buie, M. W., Bond, H. E., Johnson, J., Harrison, T., and Gehr, R. D.: 1989, *IAUC* **4786**, 1
- Malzac, J.: 2012, *International Journal of Modern Physics Conference Series* **8**, 73
- Malzac, J. and Belmont, R.: 2008, in *Microquasars and Beyond*, p. 7
- Markoff, S., Nowak, M. A., and Wilms, J.: 2005, *ApJ* **635**, 1203
- McClintock, J. E. and Remillard, R. A.: 2006, *Black hole binaries*, pp 157–213

- Meegan, C., Lichti, G., Bhat, P. N., Bissaldi, E., Briggs, M. S., Connaughton, V., Diehl, R., Fishman, G., Greiner, J., Hoover, A. S., van der Horst, A. J., von Kienlin, A., Kippen, R. M., Kouveliotou, C., McBreen, S., Paciesas, W. S., Preece, R., Steinle, H., Wallace, M. S., Wilson, R. B., and Wilson-Hodge, C.: 2009, *ApJ* **702**, 791
- Miller-Jones, J. C. A., Jonker, P. G., Dhawan, V., Brisken, W., Rupen, M. P., Nelemans, G., and Gallo, E.: 2009, *ApJL* **706**, L230
- Miyakawa, T., Yamaoka, K., Homan, J., Saito, K., Dotani, T., Yoshida, A., and Inoue, H.: 2008, *PASJ* **60**, 637
- Miyamoto, S., Kimura, K., Kitamoto, S., Dotani, T., and Ebisawa, K.: 1991, *ApJ* **383**, 784
- Motta, S., Beardmore, A., Oates, S., Sanna, N. P. M. K. A., Kuulkers, E., Kajava, J., and Sanchez-Fernandez, C.: 2015, *The Astronomer's Telegram* **7665**, 1
- Narayan, R. and Yi, I.: 1994, *ApJL* **428**, L13
- Natalucci, L., Fionchi, M., Bazzano, A., Ubertini, P., Roques, J.-P., and Jourdain, E.: 2015, *ApJL* **813**, L21
- Pietrini, P. and Krolik, J. H.: 1995, *ApJ* **447**, 526
- Rana, V., Loh, A., Corbel, S., Tomsick, J. A., Chakrabarty, D., Walton, D. J., Barret, D., Boggs, S. E., Christensen, F. E., Craig, W., Fuerst, F., Gandhi, P., Grefenstette, B. W., Hailey, C., Harrison, F. A., Madsen, K. K., Rahoui, F., Stern, D., Tendulkar, S., and Zhang, W. W.: 2015, *ArXiv e-prints*
- Remillard, R. A. and McClintock, J. E.: 2006, *ARA&A* **44**, 49
- Rodriguez, J., Cadolle Bel, M., Alfonso-Garzón, J., Siebert, T., Zhang, X.-L., Grinberg, V., Savchenko, V., Tomsick, J. A., Chenevez, J., Clavel, M., Corbel, S., Diehl, R., Domingo, A., Gouiffès, C., Greiner, J., Krause, M. G. H., Laurent, P., Loh, A., Markoff, S., Mas-Hesse, J. M., Miller-Jones, J. C. A., Russell, D. M., and Wilms, J.: 2015, *A&A* **581**, L9
- Roques, J.-P., Jourdain, E., Bazzano, A., Fionchi, M., Natalucci, L., and Ubertini, P.: 2015, *ApJL* **813**, L22
- Sharma, P., Quataert, E., Hammett, G. W., and Stone, J. M.: 2007, *ApJ* **667**, 714
- Siebert, T., Diehl, R., Greiner, J., Krause, M. G. H., Beloborodov, A. M., Bel, M. C., Guglielmetti, F., Rodriguez, J., Strong, A. W., and Zhang, X.: 2016, *Nature* **531**, 341
- Sobolewska, M. A., Papadakis, I. E., Done, C., and Malzac, J.: 2011, *MNRAS* **417**, 280
- Spitzer, L.: 1962, *Physics of Fully Ionized Gases*
- Sunyaev, R. A. and Titarchuk, L. G.: 1980, *A&A* **86**, 121
- Titarchuk, L.: 1994, *ApJ* **434**, 570
- Wilson-Hodge, C. A., Case, G. L., Cherry, M. L., Rodi, J., Camero-Arranz, A., Jenke, P., Chaplin, V., Beklen, E., Finger, M., Bhat, N., Briggs, M. S., Connaughton, V., Greiner, J., Kippen, R. M., Meegan, C. A., Paciesas, W. S., Preece, R., and von Kienlin, A.: 2012, *ApJS* **201**, 33

Table 2. V404 Cyg Spectral Modeling Results

bn	Dur [s]	Reflection amp. <sup>a</sup>	e <sup>-1</sup> Temp. <sup>a</sup> [keV]	Seed $\gamma$ Temp. <sup>a</sup> [keV]	Optical Depth <sup>a</sup>	Luminosity <sup>a,b</sup> 10 <sup>37</sup> [erg cm <sup>-2</sup> ] 10-1000 keV	$\chi^2/\text{dof}$	e <sup>-1</sup> Temp. <sup>c</sup> [keV]	Seed $\gamma$ Temp. <sup>c</sup> [keV]	Optical Depth <sup>c</sup>	Luminosity <sup>b,c</sup> 10 <sup>37</sup> [erg cm <sup>-2</sup> ] 10-1000 keV	$\chi^2/\text{dof}$
150615791	31	fixed at $\Omega/2\pi = 1$	uncons	fixed at 1.0	uncons	5.7 ± 1.1	1.12	uncons	7.36 ± 0.91	uncons	5.5 ± 1.0	1.12
150615798	149	fixed at $\Omega/2\pi = 1$	24.8 ± 3.4	fixed at 1.0	1.67 ± 0.29	4.80 ± 0.20	1.26	21.7 ± 3.1	4.54 ± 0.30	1.71 ± 0.34	4.77 ± 0.24	1.26
150616734	14	fixed at $\Omega/2\pi = 1$	32.3 ± 5.8	fixed at 1.0	2.73 ± 0.66	4.78 ± 0.56	1.04	26.0 ± 4.5	4.5 ± 1.8	3.01 ± 0.79	4.67 ± 0.52	1.04
150616855	20	fixed at $\Omega/2\pi = 1$	47.6 ± 12.	fixed at 1.0	2.44 ± 0.63	4.6 ± 1.8	1.06	36.3 ± 6.4	3.5 ± 2.2	2.68 ± 0.59	4.41 ± 0.66	1.05
150616921	581	fixed at $\Omega/2\pi = 1$	32.5 ± 3.6	fixed at 1.0	2.47 ± 0.33	3.70 ± 0.21	0.95	28.0 ± 3.1	5.27 ± 0.80	2.38 ± 0.40	3.64 ± 0.14	0.95
150618710	162	fixed at $\Omega/2\pi = 1$	54.9 ± 19.	fixed at 1.0	1.38 ± 0.48	4.4 ± 1.7	1.11	36.7 ± 6.0	2.4 ± 1.1	1.90 ± 0.31	4.30 ± 0.39	1.10
150618763	10	fixed at $\Omega/2\pi = 1$	53.4 ± 39.	fixed at 1.0	1.0 ± 1.0	11.3 ± 4.8	1.23	48.1 ± 35.	6.6 ± 1.0	uncons	11.3 ± 5.0	1.23
150618834	173	fixed at $\Omega/2\pi = 1$	44.5 ± 3.6	fixed at 1.0	1.80 ± 0.16	8.24 ± 0.19	1.19	39.6 ± 3.3	6.46 ± 0.29	1.59 ± 0.16	8.13 ± 0.21	1.21
150619165	126	fixed at $\Omega/2\pi = 1$	24.6 ± 1.8	fixed at 1.0	3.15 ± 0.38	5.36 ± 0.18	0.89	21.8 ± 1.8	5.62 ± 0.92	2.94 ± 0.50	5.31 ± 0.15	0.89
150619173	139	fixed at $\Omega/2\pi = 1$	33.8 ± 2.9	fixed at 1.0	2.46 ± 0.24	6.12 ± 0.28	1.16	28.0 ± 2.2	4.69 ± 0.61	2.54 ± 0.28	5.97 ± 0.19	1.16
150619224	24	fixed at $\Omega/2\pi = 1$	45.6 ± 23.	fixed at 1.0	1.6 ± 1.3	5.2 ± 1.5	1.21	uncons	10.8 ± 1.8	uncons	5.5 ± 1.4	1.21
150619242	77	fixed at $\Omega/2\pi = 1$	19.5 ± 2.3	fixed at 1.0	2.63 ± 0.45	21.1 ± 1.0	1.00	18.3 ± 2.7	5.25 ± 0.71	2.36 ± 0.62	21.0 ± 1.0	1.00
150619301	248	fixed at $\Omega/2\pi = 1$	27.5 ± 13.	fixed at 1.0	1.23 ± 0.91	6.1 ± 1.9	1.20	30.3 ± 2.6	5.65 ± 0.57	uncons	6.1 ± 2.5	1.20
150619309	155	fixed at $\Omega/2\pi = 1$	24.1 ± 2.0	fixed at 1.0	2.22 ± 0.27	20.64 ± 0.45	1.35	23.2 ± 2.5	6.38 ± 0.41	1.83 ± 0.34	20.64 ± 0.69	1.36
150619316	218	fixed at $\Omega/2\pi = 1$	25.2 ± 2.1	fixed at 1.0	2.03 ± 0.24	26.39 ± 0.69	1.56	47.1 ± 24.	7.31 ± 0.21	0.55 ± 0.50	27.5 ± 10.	1.49
150619342	286	fixed at $\Omega/2\pi = 1$	27.92 ± 0.78	fixed at 1.0	2.362 ± 0.083	23.79 ± 0.26	1.46	25.45 ± 0.82	5.39 ± 0.17	2.13 ± 0.10	23.62 ± 0.25	1.50
150619352	36	fixed at $\Omega/2\pi = 1$	25.4 ± 4.2	fixed at 1.0	2.73 ± 0.62	10.8 ± 1.2	1.13	24.3 ± 5.5	6.0 ± 1.5	2.21 ± 0.85	10.8 ± 1.1	1.13
150619420	15	fixed at $\Omega/2\pi = 1$	25.2 ± 4.4	fixed at 1.0	2.95 ± 0.67	8.0 ± 1.6	1.04	20.0 ± 2.4	uncons	3.67 ± 0.71	7.8 ± 2.2	1.04
150619427	96	fixed at $\Omega/2\pi = 1$	30.8 ± 2.9	fixed at 1.0	2.37 ± 0.28	9.10 ± 0.32	1.09	26.7 ± 2.4	5.34 ± 0.61	2.31 ± 0.32	9.00 ± 0.32	1.08
150619554	103	fixed at $\Omega/2\pi = 1$	17.0 ± 2.9	fixed at 1.0	2.58 ± 0.86	12.72 ± 0.96	1.68	16.6 ± 4.2	6.6 ± 1.1	2.0 ± 1.2	12.7 ± 1.4	1.69
150619561	194	fixed at $\Omega/2\pi = 1$	27.6 ± 1.5	fixed at 1.0	1.62 ± 0.12	36.36 ± 0.43	1.60	26.5 ± 1.8	5.51 ± 0.14	1.37 ± 0.15	36.37 ± 0.56	1.61
150619570	109	fixed at $\Omega/2\pi = 1$	43.5 ± 14.	fixed at 1.0	1.47 ± 0.57	10.0 ± 2.0	0.95	35.8 ± 10.	5.38 ± 0.76	1.48 ± 0.58	9.7 ± 1.4	0.95
150619580	180	fixed at $\Omega/2\pi = 1$	38.1 ± 34.	fixed at 1.0	uncons	5.5 ± 2.5	1.22	uncons	11.0 ± 1.6	uncons	5.4 ± 2.4	1.30
150619774	516	fixed at $\Omega/2\pi = 1$	31.63 ± 0.72	fixed at 1.0	2.641 ± 0.069	19.61 ± 0.19	1.38	26.43 ± 0.58	4.75 ± 0.19	2.695 ± 0.089	19.15 ± 0.20	1.43
150620136	275	fixed at $\Omega/2\pi = 1$	24.51 ± 0.65	fixed at 1.0	3.25 ± 0.16	16.73 ± 0.26	1.33	23.22 ± 0.75	5.70 ± 0.44	2.78 ± 0.18	16.94 ± 0.27	1.25
150620154	204	fixed at $\Omega/2\pi = 1$	13.38 ± 0.49	fixed at 1.0	3.38 ± 0.16	12.9 ± 3.2	1.61	10.93 ± 0.32	1.93 ± 0.68	4.75 ± 0.29	12.88 ± 0.30	1.60
150620171	163	fixed at $\Omega/2\pi = 1$	26.1 ± 2.3	fixed at 1.0	1.77 ± 0.24	13.42 ± 0.22	1.66	47.1 ± 26.	7.51 ± 0.19	uncons	13.8 ± 6.3	1.62
150620414	244	fixed at $\Omega/2\pi = 1$	21.5 ± 1.2	fixed at 1.0	2.43 ± 0.17	22.41 ± 0.43	1.32	18.13 ± 0.96	3.95 ± 0.29	2.71 ± 0.22	22.19 ± 0.35	1.35
150620421	293	fixed at $\Omega/2\pi = 1$	16.94 ± 0.70	fixed at 1.0	2.82 ± 0.14	13.56 ± 0.59	1.38	13.65 ± 0.48	2.77 ± 0.31	3.68 ± 0.22	13.41 ± 0.21	1.37
150620429	139	fixed at $\Omega/2\pi = 1$	20.8 ± 3.0	fixed at 1.0	2.26 ± 0.40	5.09 ± 0.40	1.13	17.8 ± 2.6	3.88 ± 0.60	2.47 ± 0.53	5.05 ± 0.29	1.13
150620503	22	fixed at $\Omega/2\pi = 1$	33.5 ± 9.2	fixed at 1.0	0.96 ± 0.39	43.9 ± 6.9	1.53	33.8 ± 11.	5.37 ± 0.21	0.72 ± 0.46	43.6 ± 8.4	1.52

Table 2 continued







Table 2 (*continued*)

bn	Dur	Reflection amp. <sup>a</sup>	e <sup>-1</sup> Temp. <sup>a</sup>	Seed $\gamma$ Temp. <sup>a</sup>	Optical Depth <sup>a</sup>	Luminosity <sup>a,b</sup>	$\chi^2/\text{dof}$	e <sup>-1</sup> Temp. <sup>c</sup>	Seed $\gamma$ Temp. <sup>c</sup>	Optical Depth <sup>c</sup>	Luminosity <sup>b,c</sup>	$\chi^2/\text{dof}$
	[s]		[keV]	[keV]		10 <sup>37</sup> [erg cm <sup>-2</sup> ]		[keV]	[keV]		10 <sup>37</sup> [erg cm <sup>-2</sup> ]	
						10-1000 keV					10-1000 keV	
150627162	192	fixed at $\Omega/2\pi = 1$	42.7 $\pm$ 3.0	fixed at 1.0	1.90 $\pm$ 0.13	9.06 $\pm$ 0.97	1.15	31.9 $\pm$ 1.5	3.61 $\pm$ 0.32	2.24 $\pm$ 0.13	8.70 $\pm$ 0.19	1.13
150627978	49	fixed at $\Omega/2\pi = 1$	36.5 $\pm$ 4.7	fixed at 1.0	2.42 $\pm$ 0.31	uncons	1.16	26.9 $\pm$ 2.4	3.32 $\pm$ 0.96	2.98 $\pm$ 0.38	5.03 $\pm$ 0.26	1.18

<sup>a</sup> REFLECT\*CompTT model

<sup>b</sup> (10-1000 keV)

<sup>c</sup> CompTT model